



Co nanoparticles modified N-doped carbon nanosheets array as a novel bifunctional photothermal membrane for simultaneous solar-driven interfacial water evaporation and persulfate mediating water purification

Lingfang Cui ^{a,1}, Peifang Wang ^{a,1}, Huinan Che ^a, Xin Gao ^a, Juan Chen ^a, Bin Liu ^b, Yanhui Ao ^{a,*}

^a Key Laboratory of Integrated Regulation and Resource Development on Shallow Lakes, Ministry of Education, College of Environment, Hohai University, No.1, Xikang road, Nanjing 210098, China

^b Department of Materials Science and Engineering, City University of Hong Kong, Hong Kong SAR 999077, China



ARTICLE INFO

Keywords:

Interfacial water evaporation
Persulfate
Plasma
Weak interactions
VOCs contaminated water

ABSTRACT

Solar-driven interfacial water evaporation is an effective way to produce clean freshwater. However, it is still challenging that volatile organic compounds might enter the condensate in the evaporation process. Herein, we designed a novel bifunctional photothermal membrane (Co-N-C/CF) that can be applied for simultaneous water evaporation and persulfate mediating water purification. Due to the molecular thermal vibrations effect of carbon-based materials, plasmonic effect of Co NPs, the membrane exhibited an impressive water evaporation rate of $1.88 \text{ kg m}^{-2} \text{ h}^{-1}$ (1 sun irradiation). Furthermore, Co-N-C/CF could effectively activate persulfate for phenol (PE) removal through a non-radical reaction process. Experiments and density functional theory calculations illustrated that PE is favorable to be degraded while water molecules are easier to be converted into vapor in the photothermal evaporation process. Hence, the combination of persulfate-based oxidation and solar-driven water evaporation shows great application potential in the durable and efficient production of clean water.

1. Introduction

Fresh water shortage crisis becomes more and more serious as the population growth and industrial development [1–3]. Hence, researchers have focused on developing a variety of water treatment technologies, such as photocatalysis [4–6], solar-driven water evaporation [7–11] and so on. Particularly, as a green technology, solar-driven interfacial water evaporation has attracted extensive attention in wastewater treatment as well as in alleviating water shortage [12]. Due to the wide sunlight spectrum absorption [13], this technology can directly harvest solar energy and convert it into heat while purifying various water. Solar-driven interfacial evaporator greatly improves the evaporation rates through the interfacial evaporation process without heating bulk water below. Numerous photothermal materials have been developed, such as carbon materials [14], plasma metals [15,16] and semiconductor particles [10,17,18]. Indeed, carbon-based materials have attracted wide attention over the past years, presumably owing to its excellent light absorption, thermal stability and inexpensive [9,19]. Based on the molecular thermal vibration, it has great potential in the

field of photothermal conversion [20]. Moreover, localized surface plasma resonance (LSPR) of gold (Au), silver (Ag), cobalt (Co) and nickel (Ni) nanoparticles (NPs) is also a powerful way to transform light into thermal energy [21,22]. That is to say, the energy of incident light can generate high-energy electrons on the surface of NPs [9,23]. Due to the high-energy electrons, the temperature of NPs increases rapidly, which is conducive to photothermal conversion. Therefore, metal NPs encapsulated on carbon-based materials have broad prospects in the field of photothermal evaporation.

Generally, the temperature of the air-water interface can reach 40–70 °C under 1 sun irradiation, which may cause water quality safety issues since the volatile organic compounds (VOCs) such as phenol (PE) are more favorable enriched into the condensed water [7,24]. Undoubtedly, the current solar-driven interfacial water evaporation is challenged by the VOCs problem. One of the feasible ways is to degrade the VOCs before evaporation [12]. However, traditional photothermal materials cannot solve this problem effectively. It is found that the evaporators with photodegradation abilities could oxidize organics, purify polluted water, thus produce purified water rapidly [25]. For

* Corresponding author.

E-mail address: andyao@hhu.edu.cn (Y. Ao).

¹ The two authors contribute equally to the work.

example, Shi et al. designed a multi-functional honeycomb ceramic plate, which can remove VOCs in the distillate water through a heterogeneous photo-Fenton reaction while solar distillation [7]. Ye et al. explored a method for preventing VOCs entering condensed water by using activated persulfate to make good use of interfacial solar distillation [26]. Although researchers have achieved certain progress on the control of VOCs, they have not been thoroughly studied during the solar evaporation process. It was reported that carbon-based materials showed excellent organic degradation efficiency in persulfate activation [27,28]. Besides, metal NPs encapsulated in carbon materials would transfer photoinduced hot electrons from metal NPs to carbon materials, improving the overall electron transfer ability of the composites, and thus enhancing the degradation rate [29]. However, there is no work focused on these issues in the field of solar-driven interfacial water evaporation.

Herein, we designed a novel bifunctional photothermal membrane for purifying water from VOCs contaminated water. The cobalt nanoparticles (Co NPs) were encapsulated in N-doped carbon framework growing on carbon fiber cloth (Co-N-C/CF) ([Scheme 1](#)). This system achieved a sustained water evaporation rate of $1.88 \text{ kg m}^{-2} \text{ h}^{-1}$ and a solar-vapor efficiency of $\sim 87\%$ under 1 sun irradiation. The water in the membrane had a reduced vaporization enthalpy. Meanwhile, the membrane could effectively activate PS and achieved continuous removal of phenol (PE), avoiding the accumulation of VOCs in condensed water. Density functional theory (DFT) calculations further indicate that PE is more favorable to be degraded in the photothermal evaporation process, while water molecules are easier to be converted into vapor for evaporation. This bifunctional photothermal membrane provides a promising solution for preventing VOCs entering condensed freshwater in solar-driven clean water generation.

2. Experimental procedures

2.1. Chemicals

All chemicals used in this study are of analytic grade. Cobaltous nitrate hexahydrate ($\text{Co}(\text{NO}_3)_2 \cdot 6\text{H}_2\text{O}$), urea ($\text{CO}(\text{NH}_2)_2$), melamine ($\text{C}_3\text{H}_6\text{N}_6$), potassium persulfate (PS) were purchased from Aladdin and used without further purification.

2.2. Fabrication of the Co-N-C nanosheet array on CF

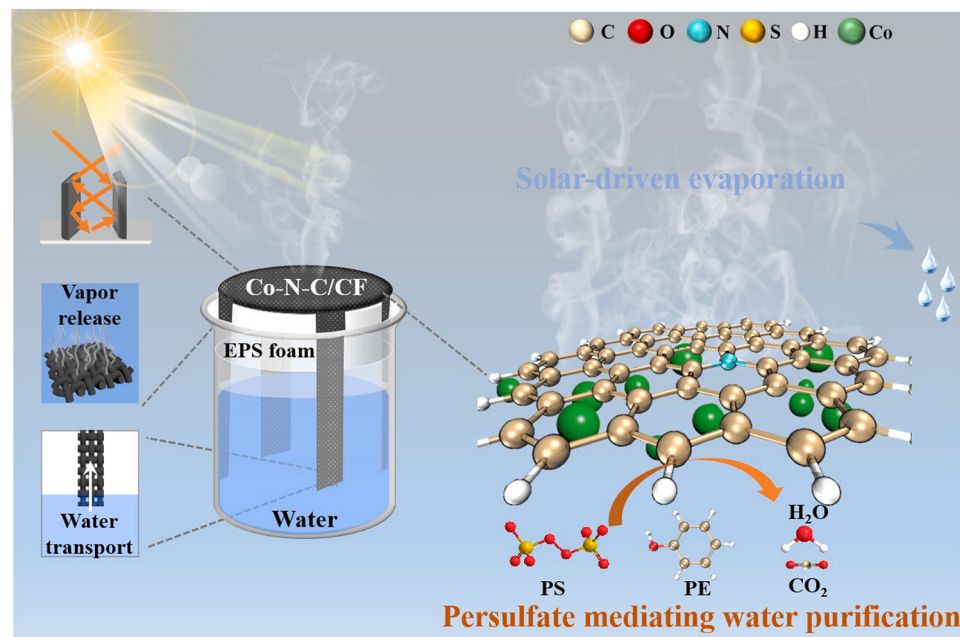
Carbon fiber cloth (CF, WOS1009 from CeTech) was ultrasonic cleaned by acetone, HCl, ethanol and deionized water, then dried at 60°C overnight. $\text{Co}(\text{NO}_3)_2 \cdot 6\text{H}_2\text{O}$ (2.5 mmol) and $\text{CO}(\text{NH}_2)_2$ (14 mmol) was dissolved in 50 mL of methanol and continuously stirred to form a transparent solution. CF and the as-obtained solution were transferred into a 100 mL Teflon-lined stainless-steel autoclave. The autoclave was maintained at 120°C for 12 h. The CF with Co-LDH nanosheet array was obtained after dried overnight. Subsequently, the Co-LDH/CF was placed in a porcelain boat filled with melamine and annealed at 650°C for 3 h at a ramping rate of 5°C min^{-1} under argon atmosphere. The Co-N-C nanosheet array on CF (Co-N-C/CF) was obtained after washing several times with acid and dried at 60°C in vacuum oven.

2.3. Materials Characterizations

X-ray diffraction (XRD) patterns were collected using a Rigaku diffractometer. The morphology of the samples was measured by scanning electron microscopy (SEM, S4800, Hitachi) and a transmission electron microscope (TEM, Tecnai G2 F30 S-TWIN). The transmittance (T) and reflectance (R) spectra (UV-vis-NIR, range = 300–2500 nm) were characterized by a UV-3600 Spectrometer (Shimadzu) equipped with an integrating sphere, and the absorption (A) spectrum was obtained by $A = 1 - T - R$. The contact angle of water droplets was carried on a contact angle meter (JY-82B Kruss DSA). XPS analysis was performed using a Thermo ESCALAB 250XI X-ray photoelectron spectroscopy. Differential scanning calorimetry (DSC) curves were performed in a NETZSCH DSC 200F3. The concentration of ions was tracked by the inductively coupled plasma spectroscopy (ICP-OES, Agilent 5110). The FLIR E6xt thermal camera was utilized to record the infrared images. Linear sweep voltammetry (LSV) and chronoamperometry measurements were performed by the CHI660D electrochemical workstation in a three-electrode system, in which Co-N-C/CF, Ag/AgCl and Pt plate as working, reference and counter electrode, respectively.

2.4. Solar-driven evaporation

The solar-driven evaporation was performed in a self-designed device ([Fig. S1](#)). In the experiment, a certain amount of wastewater was



Scheme 1. Schematic illustration of Co-N-C/CF for highly efficient solar vapor generation and persulfate mediating water purification.

put into a container and a piece of EPS foam with the diameter of 4 cm and thickness of 1.5 cm was used to cover the solution. Subsequently, the prepared film was placed on the top of the foam, and its four "legs" (1 cm * 3 cm) were immersed in the solution below, and the bulk water was transported to the top by capillary force for interface evaporation. The equipment was placed on an electronic balance to monitor quality changes in real time. The simulated solar light was provided by a xenon lamp (CEL-HXF300) with a standard AM 1.5 G optical filter. The water mass change was monitored by an electrical balance every 5 min and the surface temperature of the samples were taken by an infrared camera (FLIR E6xt). All experiments were performed under the condition (RT = 24–25 °C, RH ≈ 61 %).

2.5. Water purification test

The simultaneous solar-driven evaporation and persulfate mediating water purification were investigated using the abovementioned system under 1 sun irradiation. Before illumination, the above system was placed in dark for 1 h to reach adsorption-desorption equilibrium. Subsequently, a desired number of PS was added to the system and then put the solution under the light source. The concentrations of the pollutants in collected solution at specific time intervals were measured by a high-performance liquid chromatograph (HPLC, Waters e2695). The percentage of PE degradation is reported as C_t/C_0 [30]. C_t is the concentration of PE at each irradiated time interval, while C_0 is the initial concentration of PE before light irradiation.

2.6. Clean condensed water production

PE was selected as the model of VOCs contaminated water. The abovementioned device was then placed in a closed quartz reactor (Fig. S23) to collect clean condensed water via the bifunctional photothermal membrane. After adding the desired dosage of PS, the experiment was carried out under 1 sun irradiation. The original solution, photodegradation solution and condensed water were detected by 3D EEM fluorescence. In addition, simulated seawater (3.5 wt%) and wastewater was prepared in the presence of rhodamine B (RhB), methyl orange (MO), atrazine (ATZ), carbamazepine (CBZ), enrofloxacin (ENX). The water evaporation performance experiments were performed on the above-mentioned device. The photodegradation solution were detected by the UV-vis spectrophotometer.

2.7. Density functional theory (DFT) calculation analysis

DFT calculations were employed by Gaussian 16C. 01 program package [31]. The geometry optimization and frequency calculation were carried out by B3LYP-D3(BJ) theoretical method with the 6-31G(d) basis [32–34]. The solvent effect of H₂O was considered using the self-consistent reaction field (SCRF) based on the solvation model density (SMD) implicit solvent model [35]. Meanwhile, Hirshfeld charges, Fukui function [36,37], the highest occupied molecular orbits (HOMO), the lowest unoccupied molecular orbits (LUMO), surface electrostatic potential (ESP) of PE, localized orbital locator (LOL) [38] and interaction region indicator (IRI) [39] were calculated with Multiwfn 3.8 [40] and drawn by VMD (1.9.3 version) [41]. The adsorption energy (E_{ads}) of PE/H₂O was calculated as follows:

$$E_{ads}(\text{PE}/\text{H}_2\text{O}) = E(*\text{PE}/\text{H}_2\text{O}) - E(*) - E(\text{PE}/\text{H}_2\text{O}) \quad (1)$$

where E(*PE/H₂O), E(*) and E(PE/H₂O) are the total energy of samples with PE/H₂O on the surface, the energy of pristine samples surface and PE/H₂O, respectively.

3. Results and discussion

3.1. Structure and morphology of Co-N-C/CF

The schematic diagram of the synthesis of Co-N-C nanosheet array on CF is illustrated in Fig. 1a. First, Co-LDH nanosheet array was grown on CF via a hydrothermal method. Subsequently, the Co-N-C nanoarray was obtained by calcinating at 650 °C for 3 h under inert atmosphere, while melamine was added as the carbon/nitrogen source. Fig. 1b illustrates that the Co-LDH/CF retains the C peak at 2 theta of 26.3°, while the peaks at 10.8°, 21.5°, 34.2°, 38.1°, and 60.1° can be attributed to (003), (006), (012), (015) and (110) planes of LDH (JCPDS no. 53-0916), respectively [42,43]. By contrast, Co-N-C/CF not only exhibits the peak of C, but also clearly appears the peak of Co (JCPDS no. 15-0806). The XRD patterns also show two peaks located at 44.1° and 51.9°, which can be ascribed to the (111) and (200) planes, respectively [44]. The morphology of the prepared catalysts was characterized by SEM and TEM. As mentioned in previous report, the surface morphology of CF can affect its light absorption properties [45]. Unlike the smooth surface of CF, all Co-LDH nanosheets are perpendicular to the surface of CF in the Co-LDH/CF (Fig. S2a and b). After high-temperature calcination, the vertically grown Co-N-C nanosheets are more complete and uniform (Fig. 1c), and many nanovoids promote the interaction between light and nanosheets (Fig. S3). Particularly, the vertical array of nanosheets could increase the absorption of sunlight through multiple scattering and reflection [8]. TEM image of Co-N-C (Fig. 1d) indicates that many nanoparticles distributed on the nanosheets evenly. As shown in HRTEM image (Fig. 1e), Co NPs completely coated by carbon shells (lattice spacing = 0.339 nm), while the lattice spacing of the encapsulated Co NPs is 0.209 nm, corresponding to the (111) plane [8,46]. In previous studies, transition metal core could provide electrons to the outer carbon layer, thus promoting the interface electron transfer on the metal-carbon composites [47].

Besides, the chemical compositions of Co-N-C/CF were investigated by XPS. The measured spectrum shows the peaks assigned to Co, N, O and C, indicating the presence of Co and N in the carbon framework (Fig. S4a). The Co 2p spectrum in Fig. 2a displays two main peaks at 780.3 eV and 796.5 eV, corresponding to Co 2p_{3/2} and Co 2p_{1/2}, respectively [48]. Regarding the high-resolution N 1s spectra (Fig. 2b), Co-N-C/CF exhibit five peaks at 398.1 eV, 398.9 eV, 399.8 eV, 400.4 eV and 405.2 eV, which corresponding to pyridinic N, Co-N, pyrrolic N, graphitic N and oxidized N, respectively [49]. Obviously, it was reported that the existence of graphitic N could enhance the electron transfer from adjacent carbon atoms which could significantly improve the catalytic performance in PS activation [50]. In addition, the N doping was further proved in the C 1s spectrum as displayed in Fig. S4b, the peak locating at 286 eV is ascribed to C-N. Subsequently, the wettability was characterized by the water contact angle. As illustrated in Fig. 2c, the surface of pure CF is hydrophobic (contact angle is 108°). However, the surface of Co-N-C/CF is super-hydrophilic (contact angle is 0°). It can be expected that the excellent water transport capacity of Co-N-C/CF will enable rapid water supply and improve its solar-driven evaporation performance.

3.2. Photothermal properties of Co-N-C/CF

After the basic characterization of the catalysts, other characteristics of the prepared materials as the high-efficiency solar energy absorber were further explored. Light absorption is an important property that affects solar-vapor generation. As shown in Fig. 2d, it can be observed that pure CF exhibits lower light absorption. The Co-N-C nanosheet arrays enhance the light absorption since the scattering and reflection of sunlight and the LSPR effect of Co NPs. Notably, Co NPs can absorb sunlight through plasmonic excitation [51]. Besides, the diffuse reflection between the membrane surface and the air might reduce since the air in the wet Co-N-C/CF gap was filled with water, which was beneficial

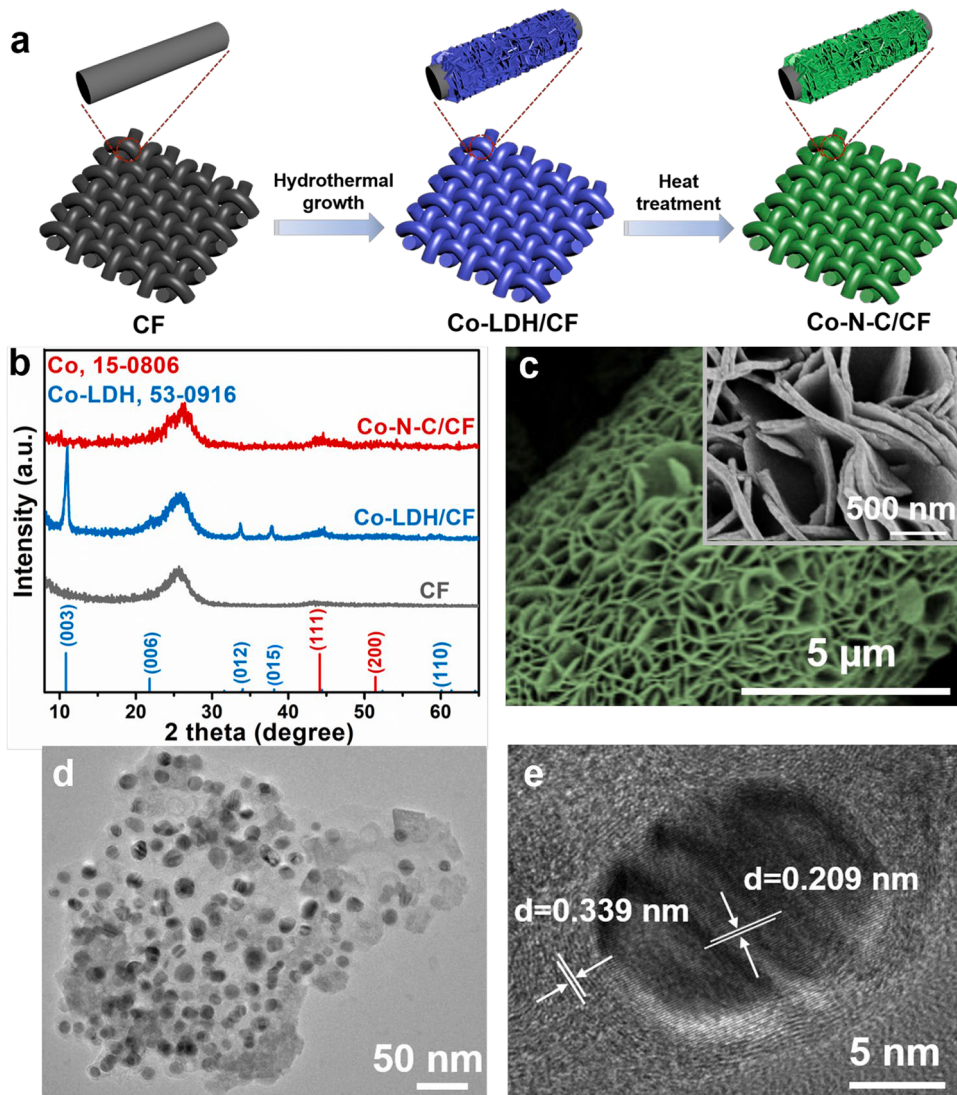


Fig. 1. (a) A schematic illustration of the fabrication process of Co-N-C array on CF. (b) XRD patterns of CF, Co-LDH/CF and Co-N-C/CF, respectively. (c) Low- and high-magnification (inset) SEM images of Co-N-C/CF. (d) TEM image and (e) HRTEM image of Co-N-C/CF.

to improve light absorption [14,52]. Fig. 2e and f demonstrate that Co-N-C/CF exhibits relatively lower reflection and transmission in the wavelength range of 300–2500 nm. In addition, Co-N-C/CF displays a rapid photothermal response under solar irradiation. Due to the excellent solar absorption, it shows a rapid temperature increase and reaches an equilibrium temperature of ~93 °C within 5 min under 1 sun irradiation (Fig. 2g). As comparison, the surface temperature of pure CF was ~88 °C within 5 min. Meanwhile, Co-N-C/CF exhibits good photo-stability (Fig. 2h), and there is no apparent change over five cycles. The surface temperatures of dry-state CF and Co-N-C/CF before and after solar illumination for 5 min was recorded by an IR camera (Fig. 2i).

3.3. Solar-driven evaporation/persulfate mediating water purification system

Inspired by the unique hierarchical array structure, good hydrophilicity and nearly 100 % sunlight absorption efficiency of Co-N-C/CF, we systematically carried out two solar-driven models: solar-driven evaporation and PS mediating water purification. The schematic diagram of the experimental setup for simultaneous solar driven evaporation and purification experiment was displayed in Fig. S1. Here, PE (5 mg L^{-1}) was selected as the model contaminant to explore the performance

because it is a common VOC. The results reveal that PE cannot be degraded in the absence of catalysts, and the PE removal is also negligible after adding PS (Fig. S5a). Subsequently, the PE removal is evaluated in the presence of light and PS (Fig. 3a). When Co-N-C/CF and PS coexist, the removal efficiency of PE reaches up to 87 % (only 33 % without PS). It is much higher than that of control pure CF (14 %). Furthermore, the rate constants (k) were calculated for comparison (Fig. 3b). The results confirm that the highest k value has achieved in Co-N-C/CF system. At the same time, no obvious deterioration after 5 cycles can be observed (Fig. S6a), illustrating its good stability. And the prepared membrane exhibits good degradation performance for different pollutants (Figs. S7–S8).

On the other hand, the water evaporation performance was studied by the mass changes of the solution every 5 min (Fig. 3d). The Co-N-C/CF achieves the mass loss of 1.88 kg m^{-2} after 60 min, which is about 1.8 times as that of pure CF system. Corresponding water evaporation rates and solar-vapor efficiencies are calculated (Fig. 3e). The solar-vapor efficiency (η) was calculated using the following formula [53–55]:

$$\eta = \dot{m}h_V / C_{\text{opt}}P_0 \quad (2)$$

where \dot{m} is the mass flux, h_V is the equivalent evaporation enthalpy of the water in Co-N-C/CF evaporator. C_{opt} is the optical concentration on

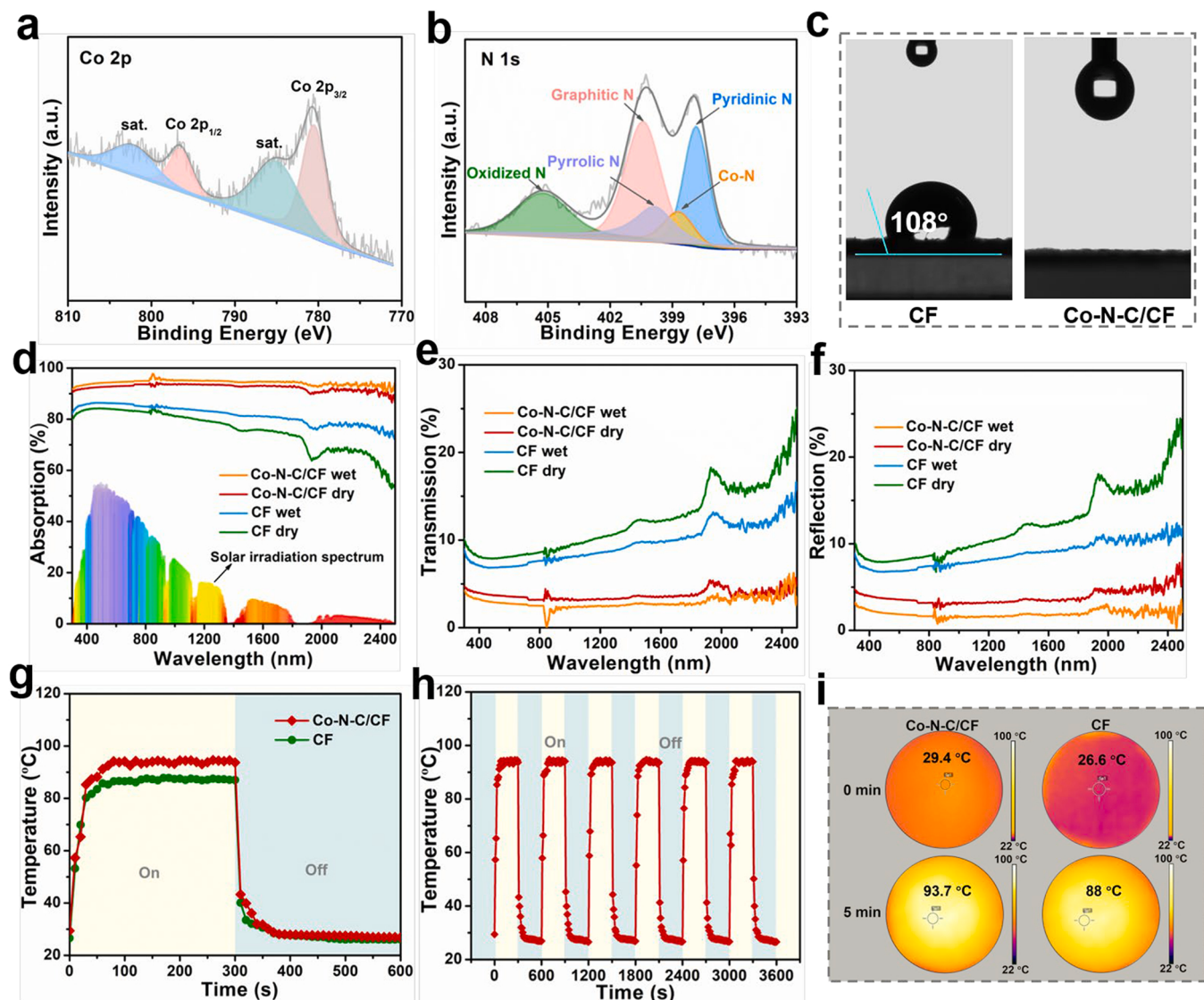


Fig. 2. (a) High-resolution XPS spectrum of Co 2p and (b) N 1s of the Co-N-C/CF. (c) Water contact angle of pure CF and Co-N-C/CF. (d) Absorption, (e) transmission and (f) reflection spectra of CF and Co-N-C/CF in dry and wet states. (g) Temperature changes in CF and Co-N-C/CF, and (h) reversible temperature changes in Co-N-C/CF under simulate solar irradiation (100 mW/cm^2). (i) Infrared thermal images of CF and Co-N-C/CF before and after solar illumination for 5 min.

the absorber surface, and P_0 refers to the solar irradiation power of 1 sun (1 kW m^{-2}). It is worth noting that evaporation estimated by the experiment and the results measured by DSC indicated that the evaporation enthalpy was reduced compared with pure bulk water (Figs. S9 and 10, Table S1). Co-N-C/CF exhibits high evaporation rate and achieved a solar-vapor efficiency of $\sim 87\%$ under 1 sun irradiation due to the low evaporation enthalpy (Fig. 3e). Due to the black appearance, the solar-vapor efficiency of pure CF reaches 47% . Besides, the vertical grown Co-N-C nanoarray on CF can increase the absorption of sunlight through multiple scattering and reflection. Moreover, the Co-N-C/CF exhibits stable evaporation performance in PE solution (5 ppm) under continuous irradiation (Fig. S6b). And the Co-N-C/CF evaporator retains high evaporation rates even in different pollutants, demonstrating its universality (Figs. S7–S8). The results verify that the outer carbon layer can prevent the direct contact between the active metal NPs and the external environment, thereby effectively improving the stability of the catalysts. To probe the effect of Co on evaporation and photo-degradation, we also prepared Co-free catalysts by direct anneal of the raw materials in the absence of Co (NC/CF). Due to the lack of Co, the removal efficiency of PE by NC/CF is much lower (Fig. S5b). It was further confirmed that Co NPs encapsulated in carbon shells could

enhance the performance in PS activation [56]. The Co NPs provides electrons to the external carbon layer, which can improve the overall electron transmission ability. In addition, the mass loss of water in NC/CF system only achieves 1.55 kg m^{-2} after 60 min (Fig. S5c). This excellent performance may be attributed to two reasons: 1) Co NPs could absorb light through plasmonic excitation [15] and then maintained a high temperature due to the photothermal effect, which could drive the reaction (Figs. S11–S12) [57]; 2) The unique nanosheet array structure could increase the photon path length through multiple reflections [10].

The high solar-vapor efficiency produced by Co-N-C/CF further illustrated the importance of thermal management. As shown in Fig. 3f, Co-N-C/CF shows a rapid increase of temperature in a short time and reaches a steady state at $\sim 59.3^\circ\text{C}$ eventually, while pure CF only reaches $\sim 51.7^\circ\text{C}$. The infrared images (Insert of Fig. 3f, Fig. S13) further verify the temperature change process. The temperature distribution of the evaporation system under irradiation was further simulated by COMSOL Multiphysics 5.6 in Figs. 3c and S14 (detailed discussion in Supporting information). Due to the heat conduction to the water layer from the four “legs” of the evaporator, only a slight heat energy lost to the water below after 60 min of solar irradiation. However, the evaporator shows a high surface temperature due to the low thermal

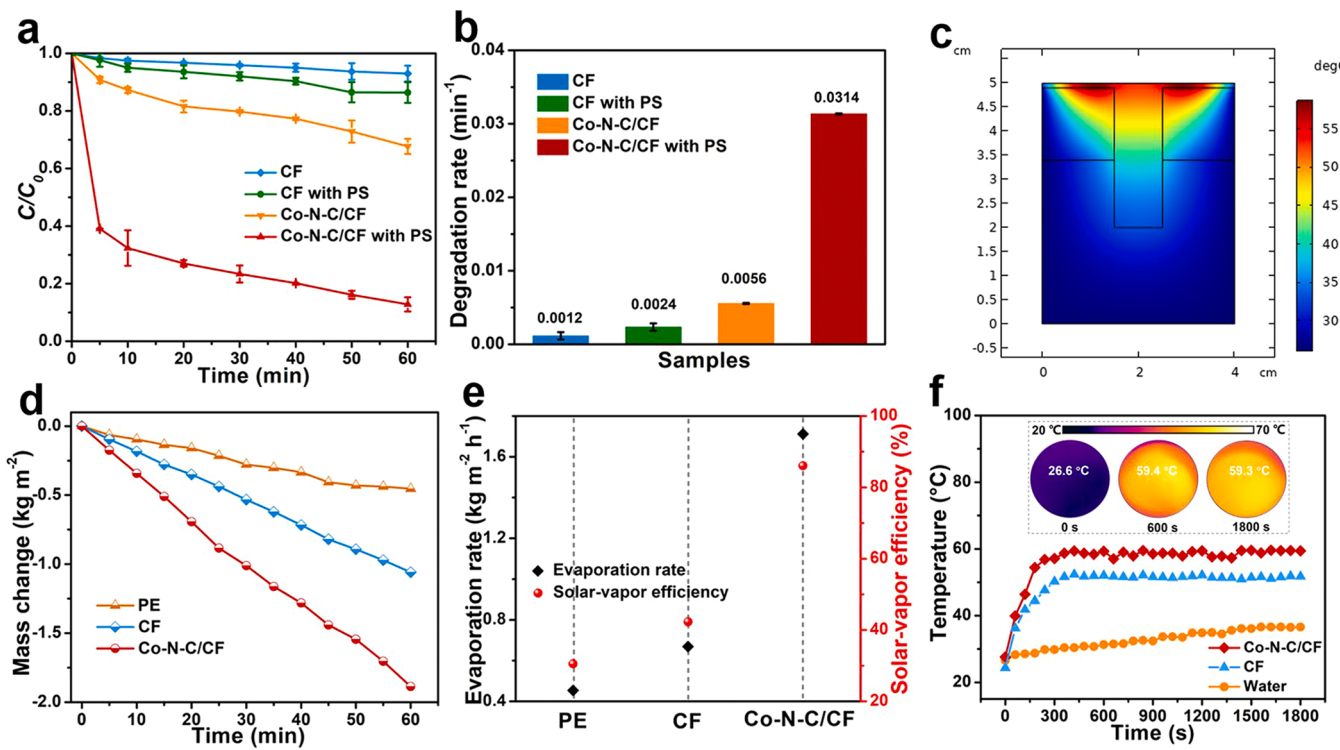


Fig. 3. (a) The removal of PE (5 mg L^{-1}) and (b) photodegradation constants (k) by CF and Co-N-C/CF with and without PS (2 mM) under non-circulating water condition. (c) Contour temperature distribution of the evaporation system by cross-sectional view under 1 sun ($t = 3600 \text{ s}$) by COMSOL Multiphysics 5.6. (d) The evaporation amount of PE solution, (e) evaporation rates and the solar-vapor efficiencies and (f) the surface temperature change of PE, CF and Co-N-C/CF under 1 sun irradiation. Insert: Infrared images of Co-N-C/CF under 1 sun irradiation.

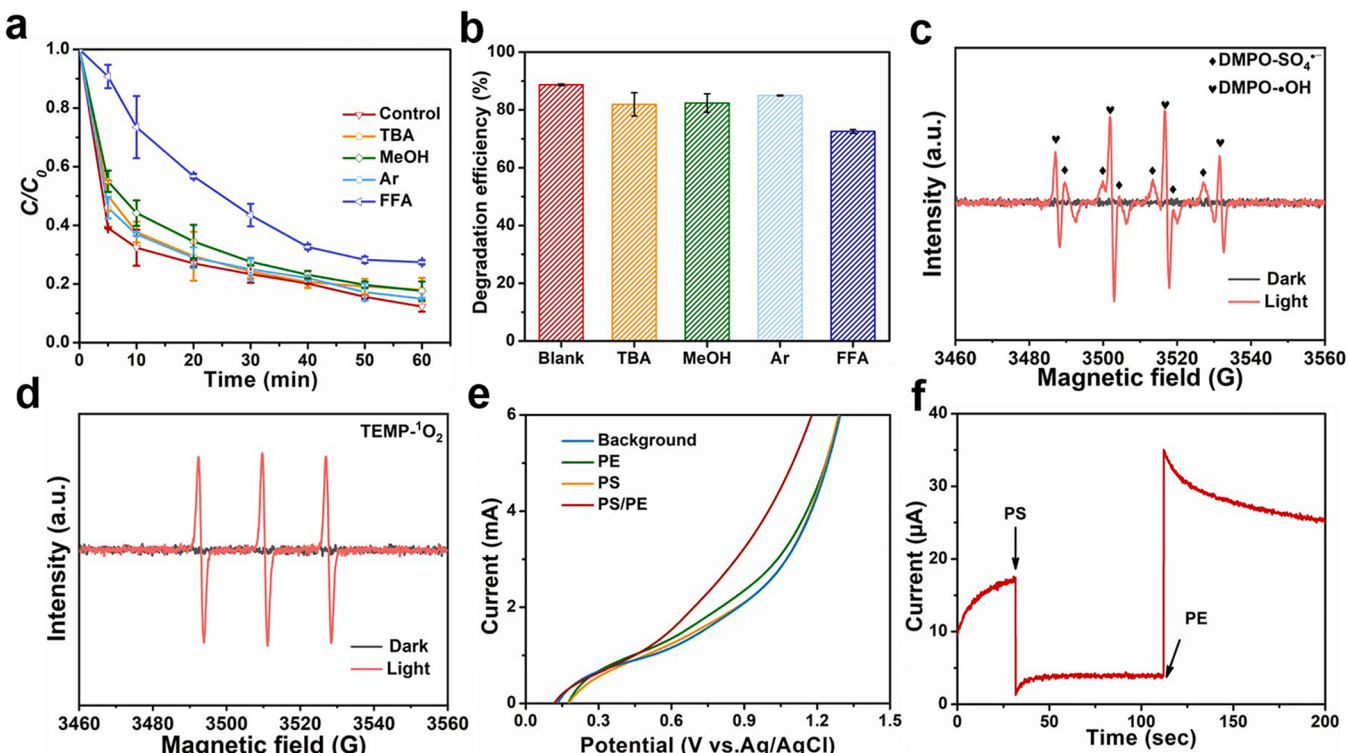


Fig. 4. (a-b) The trapping experiments of active radicals in Co-N-C/CF/light/PS system. ESR spectra of Co-N-C/CF under 1 sun irradiation: (c) DMPO-OH/SO₄, (d) TEMP-1O₂. (e) LSV measurement under different conditions at a scan rate of 20 mV s⁻¹ from 0 to 1.5 V. (f) Chronoamperometric measurements upon addition of PS and PE at Co-N-C/CF as the working electrode.

conductivity of EPS foam ($0.036 \text{ W m}^{-1} \text{ K}^{-1}$), leading to heat gathering on the top surface [58]. The effect of EPS thickness on evaporation was also studied (Fig. S15). Meanwhile, we explored the energy balance analysis that the radiation loss is 1.665 %, the convection heat loss is 1.05 %, and the conduction loss is 7.7 %. Other conditions such as light intensity, PS concentration, light and thermal effects on water evaporation and pollutant degradation were also investigated (detailed discussion in Supporting information).

3.4. Mechanism analysis

To explore the photodegradation mechanism, the trapping experiments and ESR were carried out to detect the free radicals. Basically, methanol (MeOH) is a strong scavenger for both SO_4^{\bullet} and $\bullet\text{OH}$ simultaneously; while tert-butanol (TBA), Ar, and furfuryl alcohol (FFA) could targeted quench $\bullet\text{OH}$, $\bullet\text{O}_2$ and ${}^1\text{O}_2$, respectively [59,60]. As shown in Fig. 4a and b, both MeOH, TBA and Ar exhibit little influence on PE degradation, demonstrating that the free radical process is not the

main reaction path for the degradation of PE in Co-N-C/CF/light/PS system. When FFA was added, the photodegradation rate of PE reduced to 76.5 % (Fig. 4b). DMPO was further used as the probe agent for ESR measurements to confirm the existence of radical species (SO_4^{\bullet} and $\bullet\text{OH}$). The signals of DMPO- $\bullet\text{OH}$ and DMPO- SO_4^{\bullet} can be observed (Fig. 4c), indicating that SO_4^{\bullet} and $\bullet\text{OH}$ can be produced [28,61]. The signal is obvious with the addition of TEMP (Fig. 4d), confirming that ${}^1\text{O}_2$ is generated. But we found that scavengers cannot totally inhibit the removal of PE in this system, which indicate that other route may also participate in the reaction in addition to radical oxidation.

We assumed a non-radical process involved in the removal of PE. It is confirmed that carbon-based materials can activate PS through an electron transfer pathway, where the catalysts served as the mediator to transport e^- from pollutants (electron donor) to PS (electron acceptor) [62,63]. To further monitor the electron migration in the Co-N-C/CF system, LSV and chronoamperometric measurements were used to record the current changes. Within the range of scan voltages, only a slight current change toward the Co-N-C/CF electrode are observed with the

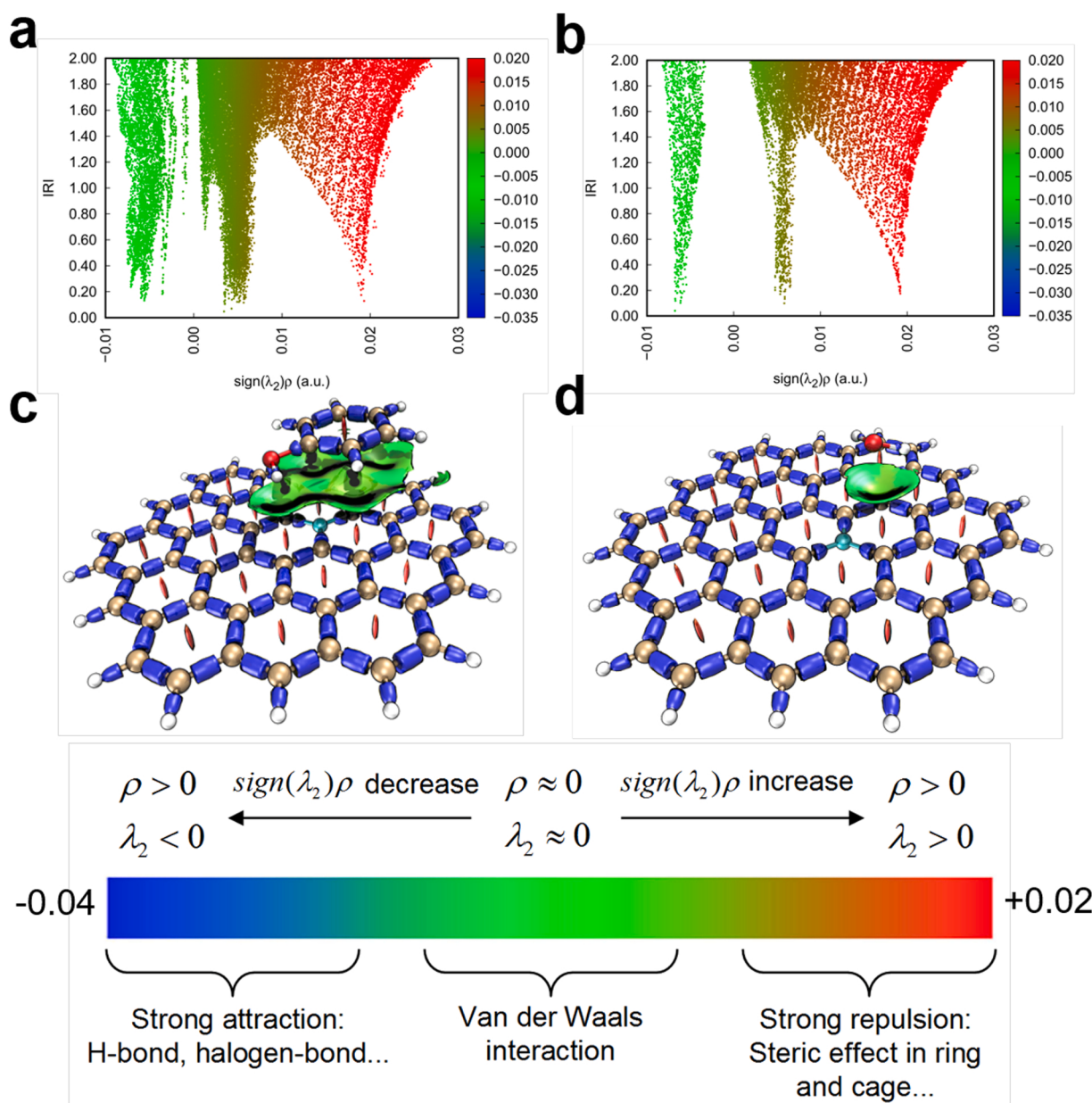


Fig. 5. Scatter maps between IRI and $\text{sign}(\lambda_2)\rho$ and isosurface maps of $\text{IRI} = 1$, (a, c) N-doped graphene + PE, (b, d) N-doped graphene+H₂O (IRI=1).

addition of PE or PS alone (Fig. 4e). However, a significant current increase is observed when both PE and PS are present. This observation indicates that the electron transfer from PE to PS occurred significantly after the close interaction of PS and PE to Co-N-C/CF surface. Similar results have appeared in previous reports [63,64]. Subsequently, chronoamperometric measurements were further carried out to confirm this phenomenon (Fig. 4f). After adding PS, a negative current appears immediately due to the electrons instantaneously transfer from Co-N-C/CF electrode to PS. Subsequently, electrons transfer from PE to Co-N-C/CF, then to PS and forms a significant positive current signal [65]. In this regard, electrons transfer form PE to activated PS [66].

As the photodegradation process is related to the molecular structure, the structure of PE (the nucleophilic and electrophilic sites) was deeply analyzed by DFT calculation (Fig. S18 and Table S2). Generally, for the materials with conjugation properties, π electrons will affect the reaction activity and sites. Since Co NPs are encapsulated in N-doped carbon layer, we choose graphene and N-doped graphene as the model of theoretical research. The isosurfaces of the localized orbital locator (LOL) of π orbital (LOL- π) in Fig. S18a and b clearly displays the global delocalization channels of electrons in pure graphene and N-doped graphene. It can be seen that electrons localized on N atom clearly for N-doped graphene compared with pure graphene. For the color-filled map of LOL- π , the reduce of LOL- π in the C-N bond region relative to the adjacent regions, which also proved the electron localization phenomenon on the N atom (Fig. S19c and d). Subsequently, the weak interaction between N-doped graphene and PE/H₂O is graphically revealed by interaction region indicator (IRI) [39,67]. The plot between IRI and $\text{sign}(\lambda_2)\rho$ for the structures (N-doped graphene+PE, N-doped graphene+H₂O) is shown in Fig. 5a and b, in which each spike relates to an IRI minimum. The corresponding IRI maps in Fig. 5c and d further reveal the interaction regions. It is obvious that there is strong π - π interaction between N-doped graphene and PE, so the isosurface presents the characteristic of van der Waals interaction. This weak interaction contributes to the formation of electron transfer between the catalysts and pollutants in the process of photodegradation, and it has a strong tendency to adsorb small molecules [39,68]. Similarly, the van der Waals interaction also exist between N-doped graphene and H₂O in this system.

Based on the above analysis, the possible mechanism of PS mediating

water purification is proposed in Fig. 6a. On the one hand, Co NPs encapsulated in N-doped carbon frameworks promote the decomposition of PS to generate $^1\text{O}_2$, which act as the main active species to photodegrade PE [50,69]. On the other hand, Co NPs strongly absorbed light and generate high-energy electrons on their surfaces under solar irradiation due to the LSPR effect. Co NPs can inject active valence electrons into the carbon layer and enhance the overall electron transfer ability of Co-N-C [47,70]. After PS is put into the system, the peroxide O-O bond in PS is activated and then forming a metastable complex [71]. Subsequently, the adsorbed PE is oxidized by providing electrons to the complex through a non-radical manner. To better explain the mechanism of VOCs removal, optimized configurations of water and PE adsorbed on N-doped graphene through DFT simulation calculation and the corresponding adsorption energies (E_{ads}) are shown in Fig. 6b. The results show that the E_{ads} of the PE on N-doped graphene (-0.66 eV) is significantly higher than that H₂O on N-doped graphene (-0.20 eV), which also indicated the N-doped carbon layer has a higher chemical affinity to PE. In general, the prepared Co-N-C/CF membrane had selective permeability to water and PE in the process of photothermal evaporation. Due to the weak interaction and the strong binding ability between the material and PE, PE is easier to be degraded by combining with the material in the evaporation process, while water molecules are easy to be converted into vapor for evaporation.

3.5. The Co-N-C/CF evaporator for clean condensed water production

In the previous works, VOCs would evaporate into the condensed water along with the water during the evaporation process of the traditional evaporator, which resulted in the collected condensed water being impure. Studies have shown that the treatment of VOCs has become an important issue in solar evaporation treatment due to the enrichment of VOCs [72]. In contrast, the evaporator with the activated PS effect could degrade organic pollutants quickly, so these systems could collect cleaner water and purify contaminated water at once. To prove the application of the Co-N-C/CF evaporator in water purification, a simulated seawater and contaminant solution was employed. RhB, MO, ATZ, CBZ and ENX were also added to the water as models to further evaluate the wastewater treatment capacities of the Co-N-C/CF evaporator. As shown in Fig. S20, the residual contaminants in the obtained condensed water were negligible. In addition, we also used 3D EEM PL spectra to study the changes of organics in solution. The concentration of organic compounds is high before PE degradation (Fig. 7a). After 1 sun irradiation, the organic compounds of the corresponding photodegradation solution and condensed water by interfacial evaporation are greatly removed (Fig. 7b and c). Therefore, it is believed that Co-N-C/CF combined with PS will be an excellent solar evaporator for generating more fresh water. As shown in Fig. 7d, the concentrations of Na⁺, K⁺, Mg²⁺ and Ca²⁺ significantly decrease by three to four orders of magnitude, and reduced to $\sim 1 \text{ mg L}^{-1}$. In addition, the purified water meets the drinking water standards of World Health Organization (WHO). Salt accumulation is an unavoidable problem during solar-driven water evaporation. As seen from Fig. 7e and Fig. S21, the evaporation rates of Co-N-C/CF evaporator for 0.8 wt%, 3 wt%, 7 wt% and 10 wt% of simulated seawater reached 1.78, 1.67, 1.53 and 1.42 kg m⁻² h⁻¹. And the evaporation rates with different salinity show a decreasing trend under 1 sun irradiation for 5 h, which can attribute to the colligative property [73–75] of the solution. Specifically, the increase in salt concentration during evaporation process will cause some of the solute molecules to take up spaces at the surface of the liquid, which will limit the number of solvent molecules located at the surface. In this scenario, only the solvent molecules located at the surface can be effectively evaporated, the presence of the solute lowers the number of solvent molecules which escape to air, thus lowering the equilibrium vapor pressure. The lowering of the vapor pressure of water in a solution is proportional to the mole fraction of the solute. Therefore, the evaporation rates show a slight decreasing trend with different salinity due to

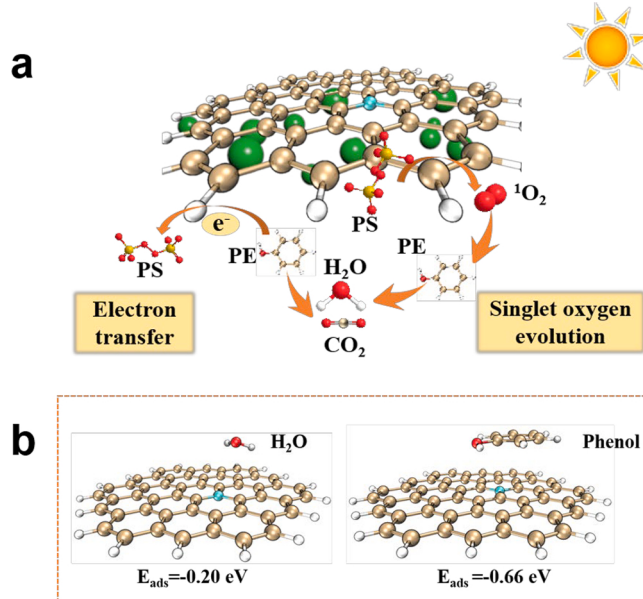


Fig. 6. Schematic diagram of employing the Co-N-C/CF evaporator for solar-driven water purification: (a) overall PS mediating photodegradation mechanism of Co-N-C; (b) the adsorption energies of water and PE onto N-doped graphene.

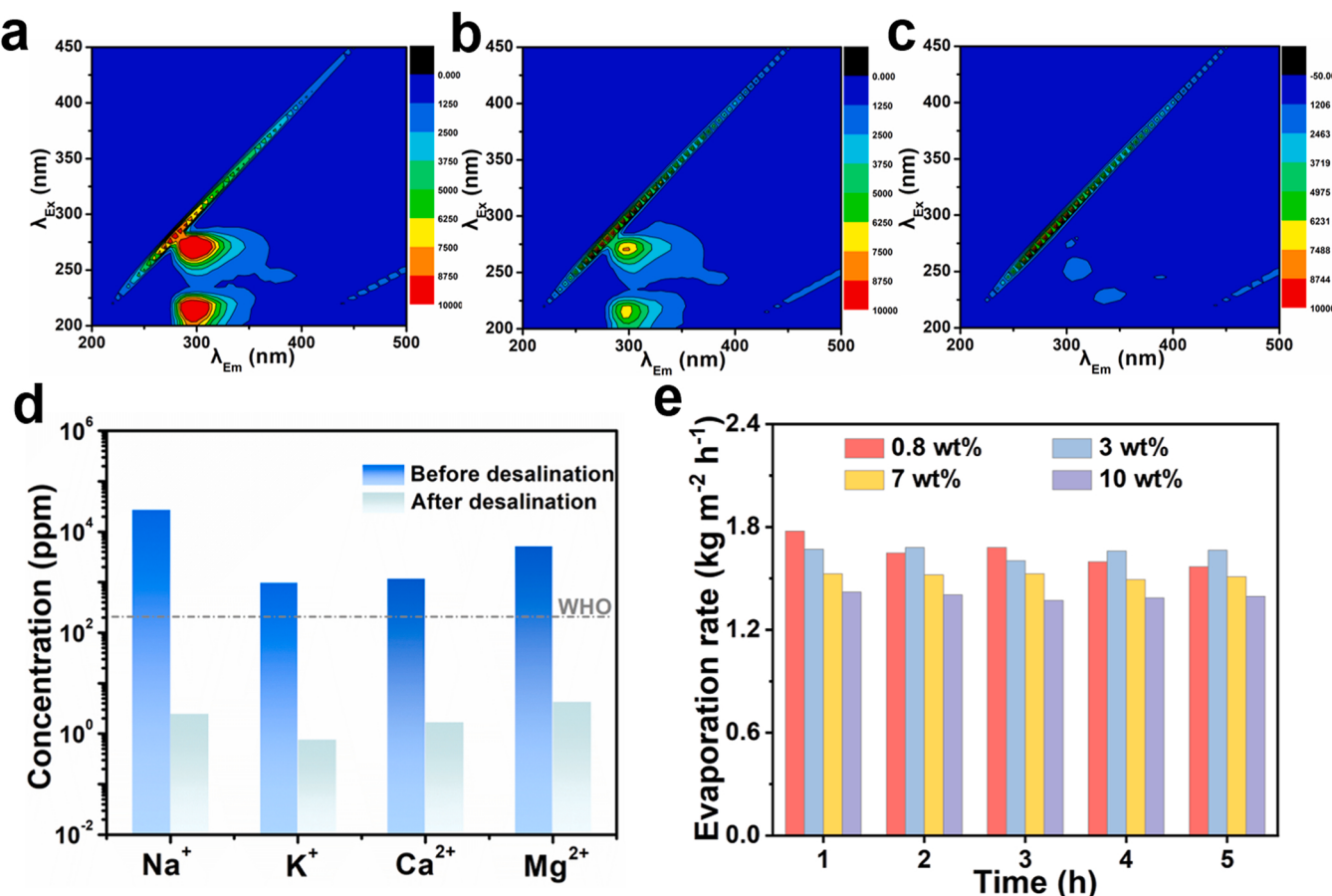


Fig. 7. 3D EEM PL spectra of the PE solution after 1 sun solar irradiation: (a) the original solution; (b) bulk water and (c) condensed water by interfacial evaporation using the simulated water collection device. (d) Salinities (the weight percentage of ions) of Na⁺, K⁺, Mg²⁺ and Ca²⁺ before and after desalination. (e) Reusability of Co-N-C/CF evaporator under 1 sun irradiation for 5 h with different salinity.

the decreased vapor pressure of the NaCl solution. It is extremely important for solar-driven evaporators to have excellent salt rejection capabilities. Fig. S22 demonstrates the exceptional salt-rejecting capabilities of the Co-N-C/CF evaporator. 1.5 g of NaCl diffused rapidly from the upper surface of the film into the bulk water within 15 min, further verifying its excellent water transport capacity and excellent salt-rejection ability, which benefiting from its vertical array structure.

4. Conclusion

In conclusion, we reported a novel bifunctional photothermal membrane (Co-N-C/CF) for simultaneous solar-driven interfacial water evaporation and persulfate mediating water purification. Compared with pure CF, the vertically grown carbon nanosheets in Co-N-C/CF enhanced multiple light reflection and light scattering, leading to strong light absorption (94 %) and exceptional salt-rejecting capabilities. The Co-N-C/CF produced clean water through solar-driven interfacial water evaporation with an evaporation rate of 1.88 kg m⁻² h⁻¹ and a solar-vapor efficiency of ~ 87 % under 1 sun irradiation. In addition, the Co-N-C/CF could effectively activate PS and achieved continuous removal of PE. Due to the weak interactions between the samples and organic molecules, Co-N-C/CF exhibited excellent removal efficiencies and water evaporation rates for VOCs, dyes and antibiotic wastewater. From the theoretical calculation based on DFT, PE is more favorable to be degraded by combining with the materials in the photothermal evaporation process, while water molecules are easier to be converted into vapor for evaporation. Given this, persulfate mediating water purification holds the promise to combine with the interfacial evaporation processes to alleviate the crisis of water shortage.

CRediT authorship contribution statement

Lingfang Cui: Methodology, Software, Validation, Visualization, Writing – original draft. **Peifang Wang:** Validation, Visualization, Formal analysis, Writing – review & editing. **Huinan Che:** Validation, Formal analysis. **Xin Gao:** Calculation. **Juan Chen:** Formal analysis. **Bin Liu:** Writing – review & editing, Formal analysis. **Yanhui Ao:** Conceptualization, Writing – review & editing, Supervision, Funding acquisition, Formal analysis.

Declaration of Competing Interest

The authors declare that they have no known competing financial interests or personal relationships that could have appeared to influence the work reported in this paper.

Data Availability

Data will be made available on request.

Acknowledgements

We are grateful for grants from National Natural Science Foundation of China (51979081, 52100179), Fundamental Research Funds for the Central Universities (B210202052), National Science Funds for Creative Research Groups of China (No. 51421006), and PAPD.

Appendix A. Supporting information

Supplementary data associated with this article can be found in the online version at doi:10.1016/j.apcatb.2023.122556.

References

- [1] J. Lou, Y. Liu, Z. Wang, D. Zhao, C. Song, J. Wu, N. Dasgupta, W. Zhang, D. Zhang, P. Tao, W. Shang, T. Deng, Bioinspired multifunctional paper-based rGO composites for solar-driven clean water generation, *ACS Appl. Mater. Interfaces* 8 (23) (2016) 14628–14636, <https://doi.org/10.1021/acsami.6b04606>.
- [2] M. Zeng, M. Chen, D. Huang, S. Lei, X. Zhang, L. Wang, Z. Cheng, Engineered two-dimensional nanomaterials: an emerging paradigm for water purification and monitoring, *Mater. Horiz.* 8 (3) (2021) 758–802, <https://doi.org/10.1039/DOMH01358G>.
- [3] M. Gao, C.K. Peh, F.L. Meng, G.W. Ho, Photothermal membrane distillation toward solar water production, *Small Methods* 5 (5) (2021) 2001200, <https://doi.org/10.1002/smtd.202001200>.
- [4] M. Tang, Y. Ao, C. Wang, P. Wang, Rationally constructing of a novel dual Z-scheme composite photocatalyst with significantly enhanced performance for neonicotinoid degradation under visible light irradiation, *Appl. Catal. B Environ.* 270 (2020), 118918, <https://doi.org/10.1016/j.apcatb.2020.118918>.
- [5] C. Wang, Y. Ao, P. Wang, S. Zhang, J. Qian, J. Hou, A simple method for large-scale preparation of ZnS nanoribbon film and its photocatalytic activity for dye degradation, *Appl. Surf. Sci.* 256 (2010) 4125–4128, <https://doi.org/10.1016/j.apsusc.2010.01.095>.
- [6] Y. Wu, J. Chen, H. Che, X. Gao, Y. Ao, P. Wang, Boosting 2e⁻ oxygen reduction reaction in garland carbon nitride with carbon defects for high-efficient photocatalysis-self-fenton degradation of 2, 4-dichlorophenol, *Appl. Catal. B Environ.* 307 (2022), 121185, <https://doi.org/10.1016/j.apcatb.2022.121185>.
- [7] L. Shi, Y. Shi, S.F. Zhuo, C.L. Zhang, Y. Aldrees, S. Aleid, P. Wang, Multi-functional 3D honeycomb ceramic plate for clean water production by heterogeneous photo-fenton reaction and solar-driven water evaporation, *Nano Energy* 60 (2019) 222–230, <https://doi.org/10.1016/j.nanoen.2019.03.039>.
- [8] X. Fan, Y. Yang, X. Shi, Y. Liu, H. Li, J. Liang, Y. Chen, A. MXene-based, hierarchical design enabling highly efficient and stable solar-water desalination with good salt resistance, *Adv. Funct. Mater.* 30 (52) (2020) 2007110, <https://doi.org/10.1002/adfm.202007110>.
- [9] P. Qiao, J. Wu, H. Li, Y. Xu, L. Ren, K. Lin, W. Zhou, Plasmon Ag-promoted solar-thermal conversion on floating carbon cloth for seawater desalination and sewage disposal, *ACS Appl. Mater. Interfaces* 11 (7) (2019) 7066–7073, <https://doi.org/10.1021/acsami.8b20665>.
- [10] Q. Lu, W. Shi, H. Yang, X. Wang, Nanoconfined water-molecule channels for high-yield solar vapor generation under weaker sunlight, *Adv. Mater.* 32 (42) (2020) 2001544, <https://doi.org/10.1002/adma.202001544>.
- [11] S. Lei, D. Huang, S. Liu, M. Chen, R. Ma, M. Zeng, D. Li, W. Ma, L. Wang, Z. Cheng, Templating synthesis of natural cotton-based hierarchically structured carbon hollow microfibers for high-performance solar vapor generation, *J. Mater. Chem. A* 9 (27) (2021) 15346–15354, <https://doi.org/10.1039/DITA02117F>.
- [12] X. Ma, Z. Deng, Z. Li, D. Chen, X. Wan, X. Wang, X. Peng, A photothermal and fenton active MOF-based membrane for high-efficiency solar water evaporation and clean water production, *J. Mater. Chem. A* 8 (43) (2020) 22728–22735, <https://doi.org/10.1039/DOTA08101A>.
- [13] J. Yang, X. Zhang, X. Zhang, L. Wang, W. Feng, Q. Li, Beyond the visible: bioinspired infrared adaptive materials, *Adv. Mater.* 33 (14) (2021) 2004754, <https://doi.org/10.1002/adma.202004754>.
- [14] C. Gao, J. Zhu, Z. Bai, Z. Lin, J. Guo, Novel ramie fabric-based draping evaporator for tunable water supply and highly efficient solar desalination, *ACS Appl. Mater. Interfaces* 13 (6) (2021) 7200–7207, <https://doi.org/10.1021/acsami.0c20503>.
- [15] L. Zhou, Y. Tan, J. Wang, W. Xu, Y. Yuan, W. Cai, S. Zhu, J. Zhu, 3D self-assembly of aluminum nanoparticles for plasmon-enhanced solar desalination, *Nat. Photonics* 10 (6) (2016) 393–398, <https://doi.org/10.1038/nphoton.2016.75>.
- [16] T. Zhang, F. Meng, M. Gao, W.L. Ong, K.G. Haw, T. Ding, G.W. Ho, S. Kawi, Multi-interfacial catalyst with spatially defined redox reactions for enhanced pure water photothermal hydrogen production, *EcoMat* 3 (6) (2021) e12152, <https://doi.org/10.1002/eom2.12152>.
- [17] M. Yang, Y. Xu, X. Zhang, H.K. Bisoyi, P. Xue, Y. Yang, X. Yang, C. Valenzuela, Y. Chen, L. Wang, Bioinspired photoprotective MXene-reinforced soft tubular actuators for omnidirectional light-tracking and adaptive photovoltaics, *Adv. Funct. Mater.* 32 (26) (2022) 2201884, <https://doi.org/10.1002/adfm.202201884>.
- [18] L. Wang, Q. Li, Photochromism into nanosystems: towards lighting up the future nanoworld, *Chem. Soc. Rev.* 47 (3) (2018) 1044–1097, <https://doi.org/10.1039/C7CS00630F>.
- [19] A. Pal, G. Natu, K. Ahmad, A. Chattopadhyay, Phosphorus induced crystallinity in carbon dots for solar light assisted seawater desalination, *J. Mater. Chem. A* 6 (9) (2018) 4111–4118, <https://doi.org/10.1039/C7TA10224K>.
- [20] S. Wu, H. Chen, H. Wang, X. Chen, H. Yang, S. Darling, Solar-driven evaporators for water treatment: challenges and opportunities, *Environ. Sci.: Water Res.* 7 (1) (2021) 24–39, <https://doi.org/10.1039/D0EW00725K>.
- [21] X. Yang, Y. Chen, X. Zhang, P. Xue, P. Lv, Y. Yang, L. Wang, W. Feng, Bioinspired light-fueled water-walking soft robots based on liquid crystal network actuators with polymerizable miniaturized gold nanorods, *Nano Today* 43 (2022), 101419, <https://doi.org/10.1016/j.nantod.2022.101419>.
- [22] M. Gao, C.K. Peh, L. Zhu, G. Yilmaz, G.W. Ho, Photothermal catalytic gel featuring spectral and thermal management for parallel freshwater and hydrogen production, *Adv. Energy Mater.* 10 (23) (2020) 2000925, <https://doi.org/10.1002/aenm.202000925>.
- [23] X. Guo, C. Hao, G. Jin, H. Zhu, X. Guo, Copper nanoparticles on graphene support: an efficient photocatalyst for coupling of nitroaromatics in visible light, *Angew. Chem. Int. Ed.* 53 (7) (2014) 1973–1977, <https://doi.org/10.1002/anie.201309482>.
- [24] Q. Gan, Y. Xiao, C. Li, H. Peng, T. Zhang, M. Ye, g-C₃N₄/MoS₂ based floating solar still for clean water production by thermal/light activation of persulfate, *Chemosphere* 280 (2021), 130618, <https://doi.org/10.1016/j.chemosphere.2021.130618>.
- [25] Y. Xu, J. Ma, Y. Han, J. Zhang, F. Cui, Y. Zhao, X. Li, W. Wang, Multifunctional CuO nanowire mesh for highly efficient solar evaporation and water purification, *ACS Sustain. Chem. Eng.* 7 (5) (2019) 5476–5485, <https://doi.org/10.1021/acssuschemeng.8b06679>.
- [26] Y. Xiao, C. Li, X. Zhou, N. Tao, M. Ye, Removal of typical volatile organic compounds in condensed freshwater by activated persulfate during interfacial solar distillation, *ACS ES&T Water* 1 (11) (2021) 2423–2430, <https://doi.org/10.1021/acsetswater.1c00261>.
- [27] X. Duan, H. Sun, Y. Wang, J. Kang, S. Wang, N-doping-induced nonradical reaction on single-walled carbon nanotubes for catalytic phenol oxidation, *ACS Catal.* 5 (2) (2015) 553–559, <https://doi.org/10.1021/cs5017613>.
- [28] L. Peng, Y. Shang, B. Gao, X. Xu, Co₃O₄ anchored in N, S heteroatom co-doped porous carbons for degradation of organic contaminant: role of pyridinic N-Co binding and high tolerance of chloride, *Appl. Catal. B Environ.* 282 (2021), 119484, <https://doi.org/10.1016/j.apcatb.2020.119484>.
- [29] J. Kanga, H. Zhang, X. Duan, H. Sun, C. Xand, S. Liua, S. Wang, Magnetic Ni-Co alloy encapsulated N-doped carbon nanotubes for catalytic membrane degradation of emerging contaminants, *Chem. Eng. J.* 362 (2019) 251–261, <https://doi.org/10.1016/j.cej.2019.01.035>.
- [30] M.L. Ren, Y.H. Ao, P.F. Wang, C. Wang, Construction of silver/graphitic-C₃N₄/bismuth tantalate Z-scheme photocatalyst with enhanced visible-light-driven performance for sulfamethoxazole degradation, *Chem. Eng. J.* 378 (2019), 122122, <https://doi.org/10.1016/j.cej.2019.122122>.
- [31] M. Frisch, G. Trucks, H. Schlegel, G. Scuseria, M. Robb, J. Cheeseman, G. Scalmani, V. Barone, G. Petersson, H. Nakatsuji, X. Li, M. Caricato, A. Marenich, J. Bloino, B. Janesko, R. Gomperts, B. Mennucci, H. Hratchian, J. Ortiz, A. Izmaylov, J. Sonnenberg, D. Williams-Young, F. Ding, F. Lipparini, F. Egidi, J. Goings, B. Peng, A. Petrone, T. Henderson, D. Ranasinghe, V. Zakrzewski, J. Gao, N. Rega, G. Zheng, W. Liang, M. Hada, M. Ehara, K. Toyota, R. Fukuda, J. Hasegawa, M. Ishida, T. Nakajima, Y. Honda, O. Kitao, H. Nakai, T. Vreven, K. Throssell, J. Montgomery, Jr., J. Peralta, F. Ogliaro, M. Bearpark, J. Heyd, E. Brothers, K. Kudin, V. Staroverov, T. Keith, R. Kobayashi, J. Normand, K. Raghavachari, A. Rendell, J. Burant, S. Iyengar, J. Tomasi, M. Cossi, J. Millam, M. Klene, C. Adamo, R. Cammi, J. Ochterski, R. Martin, K. Morokuma, O. Farkas, J. Foresman, D. Fox, Gaussian 16 Revision C. 01, Gaussian, Inc., Wallingford CT, 2016.
- [32] P. Stephens, F. Devlin, C. Chabalowski, M. Frisch, Ab initio calculation of vibrational absorption and circular dichroism spectra using density functional force fields, *J. Phys. Chem.* 98 (45) (1994) 247–257, [https://doi.org/10.1016/0099-2614\(94\)00605-9](https://doi.org/10.1016/0099-2614(94)00605-9).
- [33] M. Frisch, J. Pople, J. Binkley, Self-consistent molecular orbital methods 25. Supplementary functions for Gaussian basis sets, *J. Chem. Phys.* 80 (7) (1984) 3265–3269, <https://doi.org/10.1063/1.447079>.
- [34] P. Hariharan, J. Pople, The influence of polarization functions on molecular orbital hydrogenation energies, *Theor. Chim. Acta* 28 (3) (1973) 213–222, <https://doi.org/10.1007/BF00533485>.
- [35] A. Marenich, C. Cramer, D. Truhlar, Universal solvation model based on solute electron density and on a continuum model of the solvent defined by the bulk dielectric constant and atomic surface tensions, *J. Phys. Chem. B* 113 (18) (2009) 6378–6396, <https://doi.org/10.1021/jp810292n>.
- [36] R. Parr, W. Yang, Density functional approach to the frontier-electron theory of chemical reactivity, *J. Am. Chem. Soc.* 106 (14) (1984) 4049–4050, <https://doi.org/10.1021/ja00326a036>.
- [37] P. Ayers, R. Parr, Variational principles for describing chemical reactions: the Fukui function and chemical hardness revisited, *J. Am. Chem. Soc.* 122 (9) (2000) 2010–2018, <https://doi.org/10.1021/ja9924039>.
- [38] Z. Liu, T. Lu, Q. Chen, An sp-hybridized all-carboatomic ring, cyclo[18]carbon: bonding character, electron delocalization, and aromaticity, *Carbon* 165 (2020) 468–475, <https://doi.org/10.1016/j.carbon.2020.05.023>.
- [39] T. Lu, Q. Chen, Interaction region indicator: a simple real space function clearly revealing both chemical bonds and weak interactions, *Chemistry-Methods* 1 (5) (2021) 231–239, <https://doi.org/10.1002/cntd.202100007>.
- [40] T. Lu, F. Chen, Multiwfns a multifunctional wavefunction analyzer, *J. Comput. Chem.* 33 (5) (2012) 580–592, <https://doi.org/10.1002/jcc.22885>.
- [41] W. Humphrey, A. Dalke, K. Schulten, VMD: visual molecular dynamics, *J. Mol. Graph. Model.* 14 (1) (1996) 33–38, [https://doi.org/10.1016/0263-7855\(96\)00018-5](https://doi.org/10.1016/0263-7855(96)00018-5).
- [42] M. Zhang, Y. Zhang, L. Ye, B. Guo, Y. Gong, Hierarchically constructed Ag nanowires shelled with ultrathin Co-LDH nanosheets for advanced oxygen evolution reaction, *Appl. Catal. B Environ.* 298 (2021), 120601, <https://doi.org/10.1016/j.apcatb.2021.120601>.
- [43] T. Wang, X. Liu, Y. Li, F. Li, Z. Deng, Y. Chen, Ultrasonication-assisted and gram-scale synthesis of Co-LDH nanosheet aggregates for oxygen evolution reaction, *Nano Res.* 13 (1) (2020) 79–85, <https://doi.org/10.1007/s12274-019-2575-5>.

[44] H. Guo, Q. Feng, J. Zhu, J. Xu, Q. Li, S. Liu, K. Xu, C. Zhang, T. Liu, Cobalt nanoparticle-embedded nitrogen-doped carbon/carbon nanotube frameworks derived from a metal-organic framework for tri-functional ORR, OER and HER electrocatalysis, *J. Mater. Chem. A* 7 (8) (2019) 3664–3672, <https://doi.org/10.1039/C8TA11400E>.

[45] T. Li, Q. Fang, X. Xi, Y. Chen, F. Liu, Ultra-robust carbon fibers for multi-media purification via solar-evaporation, *J. Mater. Chem. A* 7 (2) (2019) 586–593, <https://doi.org/10.1039/C8TA08829B>.

[46] D. Fang, Y. Wang, C. Qian, X. Liu, X. Wang, S. Chen, S. Zhang, Synergistic regulation of polysulfides conversion and deposition by MOF-derived hierarchically ordered carbonaceous composite for high-energy lithium-sulfur batteries, *Adv. Funct. Mater.* 29 (19) (2019) 1900875, <https://doi.org/10.1002/adfm.201900875>.

[47] Y. Xue, N. Pham, G. Nam, J. Choi, Y. Ahn, H. Lee, J. Jung, S. Lee, J. Lee, Persulfate activation by ZIF-67-derived cobalt/nitrogen-doped carbon composites: kinetics and mechanisms dependent on persulfate precursor, *Chem. Eng. J.* 408 (15) (2021), 127305, <https://doi.org/10.1016/j.cej.2020.127305>.

[48] C. Li, J. Zhao, L. Xie, J. Wu, G. Li, Water adsorption and dissociation promoted by Co⁺/N-C⁺-biactive sites of metallic Co/N-doped carbon hybrids for efficient hydrogen evolution, *Appl. Catal. B Environ.* 282 (2021), 119463, <https://doi.org/10.1016/j.apcatb.2020.119463>.

[49] Y. Li, R. Cao, L. Li, X. Tang, T. Chu, B. Huang, K. Yuan, Y. Chen, Simultaneously integrating single atomic cobalt sites and Co₉S₈ nanoparticles into hollow carbon nanotubes as trifunctional electrocatalysts for Zn-Air Batteries to drive water splitting, *Small* 16 (10) (2020) 1906735, <https://doi.org/10.1002/smll.201906735>.

[50] H. Dai, W. Zhou, W. Wang, Co/N co-doped carbonaceous polyhedron as efficient peroxymonosulfate activator for degradation of organic pollutants: role of cobalt, *Chem. Eng. J.* 417 (2021), 127921, <https://doi.org/10.1016/j.cej.2020.127921>.

[51] K. Feng, S. Wang, D. Zhang, L. Wang, Y. Yu, K. Feng, Z. Li, Z. Zhu, C. Li, M. Cai, Z. Wu, N. Kong, B. Yan, J. Zhong, X. Zhang, G.A. Ozin, L. He, Cobalt plasmonic superstructures enable almost 100 % broadband photon efficient CO₂ photocatalysis, *Adv. Mater.* 32 (24) (2020) 2000014, <https://doi.org/10.1002/adma.202000014>.

[52] T. Li, Q. Fang, J. Wang, H. Lin, Q. Han, P. Wang, F. Liu, Exceptional interfacial solar evaporation via heteromorphic PTFE/CNT hollow fiber arrays, *J. Mater. Chem. A* 9 (1) (2021) 390–399, <https://doi.org/10.1039/D0TA09368H>.

[53] F. Zhao, X. Zhou, Y. Shi, X. Qian, M. Alexander, X. Zhao, S. Mendez, R. Yang, L. Qu, G. Yu, Highly efficient solar vapour generation via hierarchically nanostructured gels, *Nat. Nanotechnol.* 13 (6) (2018) 489–495, [10.1038/s41565-018-0097-z](https://doi.org/10.1038/s41565-018-0097-z).

[54] X. Zhou, F. Zhao, Y. Guo, Y. Zhang, G. Yu, A hydrogel-based antifouling solar evaporator for highly efficient water desalination, *Energy Environ. Sci.* 11 (8) (2018) 1985–1992, <https://doi.org/10.1039/c8ee00567b>.

[55] Y. Guo, H. Lu, F. Zhao, X. Zhou, W. Shi, G. Yu, Biomass-derived hybrid hydrogel evaporators for cost-effective solar water purification, *Adv. Mater.* 32 (11) (2020) 1907061, <https://doi.org/10.1002/adma.201907061>.

[56] Y. Liu, X. Chen, Y. Yang, Y. Feng, D. Wu, S. Mao, Activation of persulfate with metal-organic framework-derived nitrogen-doped porous Co@C nanoboxes for highly efficient p-chloroaniline removal, *Chem. Eng. J.* 358 (2019) 408–418, <https://doi.org/10.1016/j.cej.2018.10.012>.

[57] X. Meng, T. Wang, L. Liu, S. Ouyang, P. Li, H. Hu, T. Kako, H. Iwai, A. Tanaka, J. Ye, Photothermal conversion of CO₂ into CH₄ with H₂ over group VIII nanocatalysts: an alternative approach for solar fuel production, *Angew. Chem. Int. Ed.* 53 (43) (2014) 11478–11482, <https://doi.org/10.1002/anie.201404953>.

[58] Y. Wang, X. Wu, P. Wu, J. Zhao, X. Yang, G. Owens, H. Xu, Enhancing solar steam generation using a highly thermally conductive evaporator support, *Sci. Bull.* 66 (24) (2021) 2479–2488, <https://doi.org/10.1016/j.scib.2021.09.018>.

[59] W. Ren, L. Xiong, X. Yuan, Z. Yu, H. Zhang, X. Duan, S. Wang, Activation of peroxydisulfate on carbon nanotubes: electron-transfer mechanism, *Environ. Sci. Technol.* 53 (24) (2019) 14595–14603, <https://doi.org/10.1021/acs.est.9b05475>.

[60] R. Tang, D. Gong, Y. Deng, S. Xiong, J. Zheng, L. Li, Z. Zhou, L. Su, J. Zhao, π-π stacking derived from graphene-like biochar/g-C₃N₄ with tunable band structure for photocatalytic antibiotics degradation via peroxymonosulfate activation, *J. Hazard. Mater.* 423 (2022), 126944, <https://doi.org/10.1016/j.jhazmat.2021.126944>.

[61] Y. Zhang, W. Chu, Cooperation of multi-walled carbon nanotubes and cobalt doped TiO₂ to activate peroxymonosulfate for antipyrine photocatalytic degradation, *Sep. Purif. Technol.* 282 (2022), 119996, <https://doi.org/10.1016/j.seppur.2021.119996>.

[62] C. Nie, Z. Dai, W. Liu, X. Duan, C. Wang, B. Lai, Z. Ao, S. Wang, T. An, Criteria of active sites in nonradical persulfate activation process from integrated experimental and theoretical investigations: boron-nitrogen-co-doped nanocarbon-mediated peroxydisulfate activation as an example, *Environ. Sci.: Nano* 7 (7) (2020) 1899–1911, <https://doi.org/10.1039/D0EN00347F>.

[63] P. Shao, Y. Jing, X. Duan, H. Lin, L. Yang, W. Ren, F. Deng, B. Li, X. Luo, S. Wang, Revisiting the graphitized nanodiamond-mediated activation of peroxymonosulfate: singlet oxygenation versus electron transfer, *Environ. Sci. Technol.* 55 (23) (2021) 16078–16087, <https://doi.org/10.1021/acs.est.1c02042>.

[64] H. Lee, H. Lee, J. Jeong, J. Lee, N. Park, C. Lee, Activation of persulfates by carbon nanotubes: oxidation of organic compounds by nonradical mechanism, *Chem. Eng. J.* 266 (2015) 28–33, <https://doi.org/10.1016/j.cej.2014.12.065>.

[65] H. Lee, H. Kim, S. Weon, W. Cho, Y.S. Hwang, J. Seo, C. Lee, J.-H. Kim, Activation of persulfates by graphitized nanodiamonds for removal of organic compounds, *Environ. Sci. Technol.* 50 (18) (2016) 10134–10142, <https://doi.org/10.1021/acs.est.6b02079>.

[66] H. Che, P. Wang, J. Chen, X. Gao, B. Liu, Y. Ao, Rational design of donor-acceptor conjugated polymers with high performance on peroxydisulfate activation for pollutants degradation, *Appl. Catal. B: Environ.* 316 (2022), 121611, <https://doi.org/10.1016/j.apcatb.2022.121611>.

[67] H.N. Che, X. Gao, J. Chen, J. Hou, Y.H. Ao, P.F. Wang, Iodide-induced fragmentation of polymerized hydrophilic carbon nitride for high-performance quasi-homogeneous photocatalytic H₂O₂ production, *Angew. Chem. Int. Ed.* 60 (48) (2021) 25546–25550, <https://doi.org/10.1002/anie.202111769>.

[68] Q. Zhang, J. Chen, X. Gao, H. Che, Y. Ao, P. Wang, Understanding the mechanism of interfacial interaction enhancing photodegradation rate of pollutants at molecular level: intermolecular π-π interactions favor electrons delivery, *J. Hazard. Mater.* 430 (2022), 128386, <https://doi.org/10.1016/j.jhazmat.2022.128386>.

[69] Y. Gao, Q. Wang, G. Ji, A. Li, Degradation of antibiotic pollutants by persulfate activated with various carbon materials, *Chem. Eng. J.* 429 (2022), 132387, <https://doi.org/10.1016/j.cej.2021.132387>.

[70] M. Zeng, Y. Liu, F. Zhao, K. Nie, N. Han, X. Wang, W. Huang, X. Song, J. Zhong, Y. Li, Metallic cobalt nanoparticles encapsulated in nitrogen-enriched graphene shells: its bifunctional electrocatalysis and application in zinc-air batteries, *Adv. Funct. Mater.* 26 (24) (2016) 4397–4404, <https://doi.org/10.1002/adfm.201600636>.

[71] S. Ho, Y. Chen, R. Li, C. Zhang, Y. Ge, G. Cao, M. Ma, X. Duan, S. Wang, N. Ren, N-doped graphitic biochars from C-phycocyanin extracted Spirulina residue for catalytic persulfate activation toward nonradical disinfection and organic oxidation, *Water Res.* 159 (2019) 77–86, <https://doi.org/10.1016/j.watres.2019.05.008>.

[72] D. Xie, M. He, X.R. Li, J. Sun, J. Luo, Y. Wu, F. Cheng, Tree-inspired efficient solar evaporation and simultaneous in-situ purification of ultra-highly concentrated mixed volatile organic wastewater, *Nano Energy* 93 (2022), 106802, <https://doi.org/10.1016/j.nanoen.2021.106802>.

[73] F.P. Chinard, Colligative properties, *J. Chem. Educ.* 32 (7) (1955) 377, <https://doi.org/10.1021/ed032p377>.

[74] F. Rioux, Colligative properties, *J. Chem. Educ.* 50 (7) (1973) 490, <https://doi.org/10.1021/ed050p490>.

[75] F.C. Andrews, Colligative properties of simple solutions: solutes simply dilute the solvent; they do not cause tension in the solvent, *Science* 194 (4265) (1976) 567–571, <https://doi.org/10.1126/science.194.4265.567>.